THE JOURNAL OF PHYSICAL CHEMISTRY C

Article

pubs.acs.org/JPCC

# Isostructural Second-Order Phase Transition of $\beta$-$Bi_2O_3$ at High Pressures: An Experimental and Theoretical Study

A. L. J. Pereira,*[,†] J. A. Sans,[†] R. Vilaplana,[‡] O. Gomis,[‡] F. J. Manjón,[†] P. Rodríguez-Hernández,[§] A. Muñoz,[§] C. Popescu,[∥] and A. Beltrán[⊥]

[†]Instituto de Diseño para la Fabricación y Producción Automatizada, MALTA Consolider Team, Universitat Politècnica de València, Camí de Vera s/n, 46022 València, Spain

[‡]Centro de Tecnologías Físicas: Acústica, Materiales y Astrofísica, MALTA Consolider Team, Universitat Politècnica de València, 46022 València, Spain

[§]Departamento de Física, Instituto Univ. de Materiales y Nanotecnología, MALTA Consolider Team, Universidad de La Laguna, 38200 La Laguna, Tenerife, Spain

[∥]CELLS-ALBA Synchrotron Light Source, 08290 Cerdanyola del Valles, Barcelona, Spain

[⊥]Departament de Química Física i Analítica, MALTA Consolider Team, Universitat Jaume I, 12071 Castello, Spain

**ABSTRACT:** We report a joint experimental and theoretical study of the structural and vibrational properties of synthetic sphaerobismoite ($\beta$-$Bi_2O_3$) at high pressures in which room-temperature angle-dispersive X-ray diffraction (XRD) and Raman scattering measurements have been complemented with ab initio total-energy and lattice dynamics calculations. Striking changes in Raman spectra were observed around 2 GPa, whereas X-ray diffraction measurements evidence no change in the tetragonal symmetry of the compound up to 20 GPa; however, a significant change exists in the compressibility when increasing pressure above 2 GPa. These features have been understood by means of theoretical calculations, which show that $\beta$-$Bi_2O_3$ undergoes a pressure-induced isostructural phase transition near 2 GPa. In the new isostructural $\beta'$ phase, the $Bi^{3+}$ and $O^{2-}$ environments become more regular than those in the original $\beta$ phase because of the strong decrease in the activity of the lone electron pair of Bi above 2 GPa. Raman measurements and theoretical calculations provide evidence of the second-order nature of the pressure-induced isostructural transition. Above 20 GPa, XRD measurements suggest a partial amorphization of the sample despite Raman measurements still show weak peaks, probably related to a new unknown phase, which remains up to 27 GPa. On pressure release, XRD patterns and Raman spectra below 2 GPa correspond to elemental Bi–I, thus evidencing a pressure-induced decomposition of the sample during downstroke.

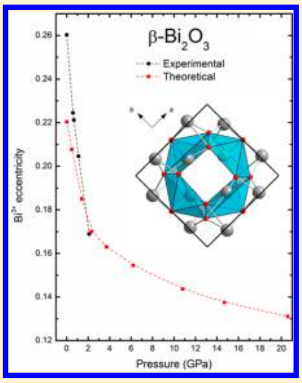


## 1. INTRODUCTION

A significant increase in the number of published works related to bismuth oxide ($Bi_2O_3$) polymorphs in the last 20 years reflects the industrial, technologic, and scientific importance of this compound. Its peculiar properties such as energy gap, refracting-index, dielectric permittivity, and photoconductivity[1−6] have made $Bi_2O_3$ suitable for a large range of applications, such as optical coatings, photovoltaic cells, microwave integrated circuits, fuel cells, oxygen sensors, and oxygen pumps.[3,7−19] Furthermore, cation-centered lone electron pairs (LEPs), as those in $Pb^{2+}$ and $Bi^{3+}$, are tremendously important for applications requiring off-centered polyhedron and their associated dipoles in ferroelectric, piezoelectric, and multiferroic materials, actuators, nonlinear materials, ionic conductors, and high-refractive index materials.

One of the most intriguing properties of $Bi_2O_3$ is the wide variety of its polymorphs. Most of them are common to other group 15 sesquioxides, like $As_2O_3$ and $Sb_2O_3$, and can be understood as derived from a defective fluorite structure by means of symmetry-breaking atomic local distortions.[20,21] The polymorphism of $Bi_2O_3$ is a complex issue that remains not understood. The most common structure of $Bi_2O_3$ found in nature is the monoclinic bismite ($\alpha$ phase; space group (S.G.) $P2_1/c$, no. 14).[22] However, several other polymorphs can be obtained depending of the preparation or annealing process. Heating $\alpha$-$Bi_2O_3$ above 730 °C results in the formation of $\delta$-$Bi_2O_3$ (S.G. $Fm\bar{3}m$, no. 225) with cubic fluorite-type structure. When $\delta$-$Bi_2O_3$ is cooled, it is possible to form two intermediate metastable phases at ambient conditions: (i) the tetragonal $\beta$ phase (S.G. $P\bar{4}2_1c$, no. 114), also known as sphaerobismoite, at ~650 °C, and (ii) the body-centered cubic $\gamma$ phase (S.G. $I23$, no. 197) at ~640 °C.[22,23] These metastable phases and also new polymorphs can be obtained by using specific synthesis conditions, by doping the sample, or if synthesized in nanometric size.[24−27] The metastable triclinic $\omega$-$Bi_2O_3$ (S.G. $P\bar{1}$, no. 2), for example, was observed when a $Bi_2O_3$ thin film is grown on a BeO substrate at 800 °C.[28] Furthermore, another metastable single crystal of orthorhombic $\varepsilon$-$Bi_2O_3$ (S.G. $Pccn$,

**Received:** August 3, 2014
**Revised:** September 5, 2014
**Published:** September 9, 2014

   dx.doi.org/10.1021/jp507826j | J. Phys. Chem. C 2014, 118, 23189−23201

no. 56) was obtained by low-temperature hydrothermal reaction at 240 °C.[29]

Besides temperature, pressure also plays an important role in the discovery of new $Bi_2O_3$ polymorphs. Starting with the $\alpha$ phase, Ghedia et al.[30] identified two different metastable polymorphs of $Bi_2O_3$ at ambient conditions after compressing the sample up to 6 GPa and heating it to 880 °C for 30 min: trigonal HP-$Bi_2O_3$ (S.G. $P31c$, no. 159) and monoclinic R-$Bi_2O_3$ (S.G. $P2_1/c$, no. 14). It must be added that a hexagonal polymorph at high pressure, named HPC-$Bi_2O_3$ (S.G. $P6_3mc$, no. 186), was recently obtained after pressurizing HP-$Bi_2O_3$.[31] On the other hand, at ambient temperature, $\alpha$-$Bi_2O_3$ experiences a pressure-induced amorphization at 20 GPa,[32,33] but it can be recrystallized into the HPC polymorph by annealing the amorphous phase at 20 GPa and 200 °C, as was recently reported.[34]

In recent years, a considerable amount of work has been devoted to the study of the catalytic properties of $Bi_2O_3$ at ambient conditions. The metastable $\beta$ phase has been shown to exhibit properties that are better than those of other phases of $Bi_2O_3$.[1,27,35,36] The unique tunnel structure of $\beta$-$Bi_2O_3$ (see Figure 1), due to the special orientation of Bi LEPs, is believed to be associated with its excellent photocatalytic activity. These tunnels can provide channels for the transfer of the photogenerated electrons and holes, preventing their excessive recombination and enabling more free carries to participate in the photodecomposition process.[37]

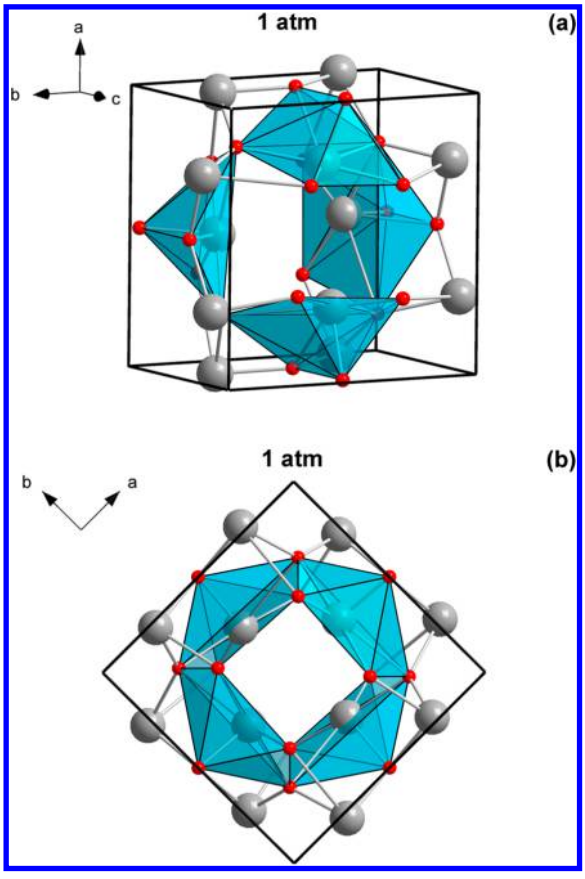


**Figure 1.** (a) Crystalline structure of tetragonal $\beta$-$Bi_2O_3$ at 1 atm. (b) The structure of $\beta$-$Bi_2O_3$ is projected along the $c$-axis to allow the observation of the atoms arranged in slightly distorted sheets. Gray balls represent Bi atoms, while red balls represent O atoms. The structure is composed by one Bi with coordination six (light blue polyhedral).

In this work, we performed a detailed experimental and theoretical study of the structural and vibrational properties of $\beta$-$Bi_2O_3$ up to 27 GPa by means of angle-dispersive X-ray diffraction (XRD) and Raman scattering (RS) measurements combined with total-energy and lattice dynamics calculations. We have found that $\beta$-$Bi_2O_3$, unlike $\alpha$-$Bi_2O_3$, undergoes a second-order isostructural phase transition (IPT) above 2 GPa which is related to a strong decrease of LEP activity with pressure. We also found that above 20 GPa the sample undergoes a phase transition accompanied with partial amorphization. The original structure is not recovered on decreasing pressure to 1 atm. Instead a partial decomposition of the sample occurs.

## 2. EXPERIMENTAL METHOD

Synthetic $\beta$-$Bi_2O_3$ samples used in the present experiments were purchased from Sigma-Aldrich Inc. with grade purity higher than 99.9%. Room-pressure XRD patterns, performed with a Rigaku Ultima IV X-ray diffractometer with Cu $K_{\alpha 1}$ + $K_{\alpha 2}$ (ratio 0.5) wavelength, and RS spectra, performed with a Horiba Jobin Yvon LabRAM HR microspectrometer, allowed us to confirm that the samples contain only a pure $\beta$ phase. Scanning electron microscopy (SEM) with a JEOL JSM6300 and energy-dispersive X-ray spectroscopy (EDX) measurements with an attached Oxford Instruments detector were also performed to study the morphology and chemical composition of the samples.

To perform high-pressure measurements, the sample was loaded together with a 16:3:1 methanol−ethanol−water mixture in a membrane-type diamond anvil cell (MDAC) with diamond culets 400 $\mu$m in diameter. Powder angle-dispersive XRD experiments were performed up to 27 GPa at room temperature in the BL04-MSPD beamline at ALBA synchrotron facility.[38] This beamline is equipped with Kirkpatrick−Baez mirrors to focus the monochromatic beam and a Rayonix CCD detector with a 165 mm diameter active area. We used a wavelength of 0.4246 Å, and the sample−detector distance during the experiment was set to 230 mm. Pressure was determined both by the luminescence of small ruby chips evenly distributed in the pressure chamber[39] and by the equation of state (EOS) of metallic Cu intentionally mixed with the sample. Integration of two-dimensional diffraction images were performed with FIT2D software,[40] while structural analysis was performed with PowderCell[41] and GSAS[42,43] program packages. To obtain information about the LEP activity, we calculated the cation eccentricity with the program IVTON[44] for both experimental and theoretical results.

Unpolarized RS measurements up to 27 GPa were performed with a Horiba Jobin Yvon LabRAM HR microspectrometer equipped with a thermoelectrically cooled multichannel charge-coupled device detector which allows a spectral resolution better than 2 $cm^{-1}$. The Raman signal was excited with a HeNe laser (6328 Å line) with a power of less than 10 mW and collected in backscattering geometry using an edge filter working in perpendicular configuration and cutting at 100 $cm^{-1}$. Raman signals down to 50 $cm^{-1}$ can eventually be detected by adjusting the angle between the edge filter and the light containing the Raman signal (provided that the Rayleigh signal is weak enough and the Raman signal is strong enough). Pressure was determined by the ruby luminescence method.[39] The frequency of the Raman-active phonons have been


dx.doi.org/10.1021/jp507826j | J. Phys. Chem. C 2014, 118, 23189−23201

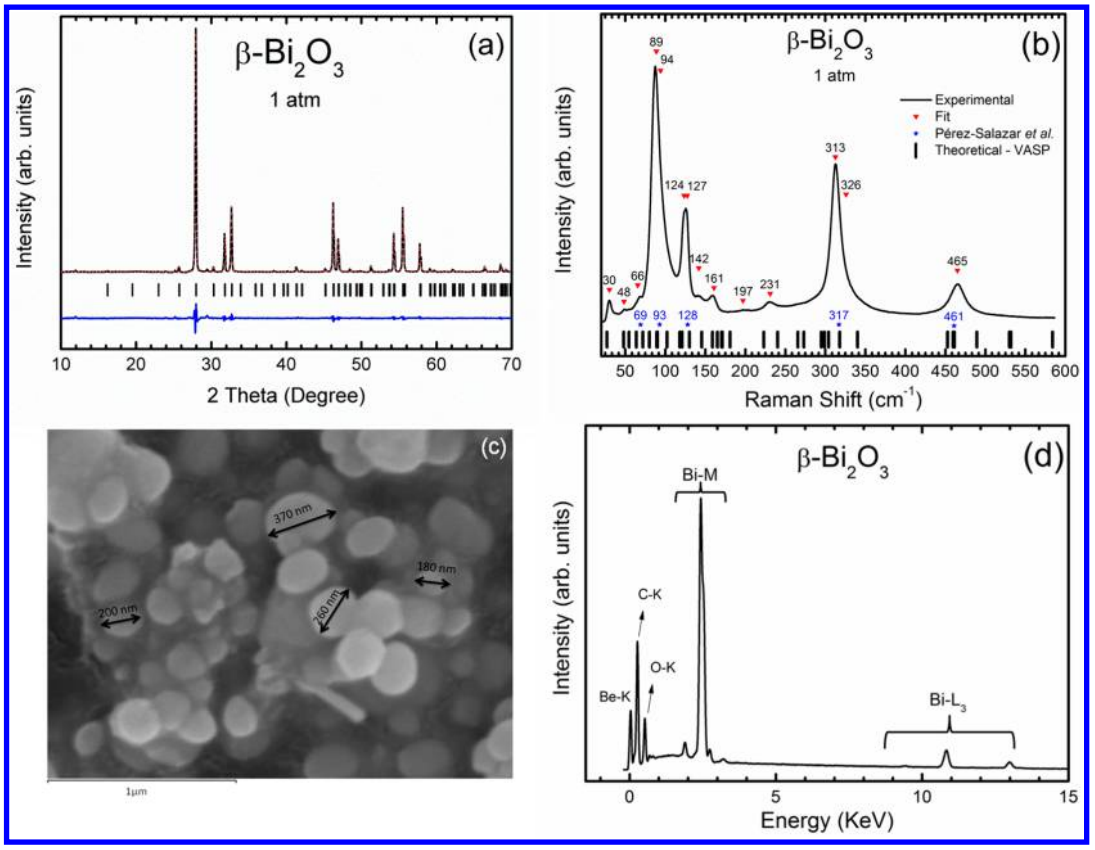


**Figure 2.** Characterization of $\beta$-$Bi_2O_3$ samples at ambient conditions: (a) powder XRD pattern showing the Rietveld refined spectrum (red dotted line) and residues (blue lower line); (b) RS spectra; (c) SEM image; and (d) EDX analysis.

experimentally analyzed by fitting Raman peaks with a Voigt profile fixing the Gaussian line width (1.6 $cm^{-1}$) to the experimental setup resolution.[45]

## 3. THEORETICAL DETAILS

Ab initio total-energy calculations were performed within the framework of density functional theory (DFT).[46] The VASP package was used to carry out calculations with the pseudopotential method and the projector augmented wave (PAW) scheme, which replace the core electrons, make smoothed pseudovalence wave functions and take into account the full nodal character of the all-electron charge density in the core region.[47] For bismuth, 15 valence electrons ($5d^{10}6s^24p^3$) were used, whereas for oxygen, 6 valence electrons ($2s^22p^4$) were used. Highly converged results were achieved by extending the set of plane waves up to a kinetic energy cutoff of 520 eV. The exchange-correlation energy was taken in the generalized gradient approximation (GGA) with the PBEsol prescription.[48] A dense Monkhorst−Pack grid of k-special points was used to perform integrations along the Brillouin zone (BZ) in order to obtain very well-converged energies and forces. At each selected volume, the structures were fully relaxed to their equilibrium configuration through the calculation of the forces on atoms and the stress tensor. In the relaxed configurations, the forces on the atoms are less than 0.006 eV/Å and deviations of the stress tensor from a diagonal hydrostatic form are less than 0.1 GPa. It should be noted that, within the DFT formalism, the theoretical pressure ($P(V)$) can be determined at the same time as the total energy ($E(V)$) because $P$ (like other derivatives of the energy) can be obtained from the calculated stress.

Lattice dynamics calculations were performed at the zone center (Γ point) of the BZ. Highly converged results on forces are required for the calculation of the dynamical matrix using the direct force constant approach.[49] The construction of the dynamical matrix at the Γ point of the BZ involves separate calculations of the forces in which a fixed displacement from the equilibrium configuration of the atoms within the primitive cell is considered. The number of such independent displacements in the analyzed structures is reduced because of crystal symmetry. Diagonalization of the dynamical matrix provides the normal-mode frequencies. Moreover, these calculations allow one to identify the symmetry and eigenvectors of the vibrational modes in each structure at the Γ point.

## 4. RESULTS

### 4.1. Characterization of $\beta$-$Bi_2O_3$ at Ambient Pressure.

The tetragonal structure of $\beta$-$Bi_2O_3$ at room pressure has a distorted defect-fluorite structure with one Bi atom located at an 8*e* Wyckoff site and two O atoms located at 8*e* and 4*d* Wyckoff sites. In this structure, Bi is 6-fold coordinated and the polyhedron surrounding Bi resembles a distorted pyramid with Bi−O bond lengths varying from 2.09 to 2.72 Å (see Figure 1a). Curiously, Bi and O atoms are arranged in slightly distorted sheets parallel to the plane (001) as in a layered material (see Figure 1b). The formation of atomic layers seems to be a common feature in many Bi-related compounds, like the polymorphs $\alpha$-$Bi_2O_3$ and HPC-$Bi_2O_3$,[33] $Bi_2S_3$,[50] and some recently discovered topological insulators based on Bi, like $Bi_2Se_3$, $Bi_2Te_3$, and $Bi_4Te_3$. As can be observed in Figure 1b, the atomic configuration in the $\beta$-$Bi_2O_3$ structure is strongly


dx.doi.org/10.1021/jp507826j | J. Phys. Chem. C 2014, 118, 23189−23201

asymmetric and results in the formation of empty tunnels due to the intersection of the Bi LEPs at certain locations.

The crystalline structure of the studied sample was characterized at room conditions by means of XRD, RS, EDX, and SEM measurements. Panels a and b of Figure 2 show the XRD pattern and RS spectrum obtained for $\beta$-$Bi_2O_3$ at room pressure, respectively. The XRD pattern agrees well with the JCPDS data card no. 78-1793. The measured lattice parameters at 1 atm are $a$ = 7.74002(5) Å and $c$ = 5.62671(7) Å, yielding a unit-cell volume $V_0$ = 337.08(5) Å$^3$. These values are in agreement with our ab initio calculations for the $\beta$ phase, where we have found that $V_0$ is 0.6% underestimated in comparison with the experimental values. These values are also in good agreement with those previously found in the literature.[51]

Regarding the lattice dynamics of $\beta$-$Bi_2O_3$, there are four formula units in the primitive cell; therefore, there are 60 normal modes of vibration at zone center whose mechanical decomposition is

$$\Gamma = 7A_1(R) + 7A_2 + 7B_1(R) + 7B_2(R, IR) + 16E(R, IR)$$

where E modes are doubly degenerated, $A_2$ modes are silent, $B_1$ modes are Raman-active (R), and $B_2$ and E are polar modes which are both Raman and infrared-active (IR). Therefore, there are 37 modes ($\Gamma$ = 7 $A_1$ + 7 $B_1$ + 7 $B_2$ + 16 E), 21 IR ($\Gamma_{IR}$= 6 $B_2$ + 15 E), and two acoustic modes ($\Gamma_{acoustic}$ = $B_2$ + E). The polar modes also show a transversal optic−longitudinal optic (TO-LO) splitting; however, such a splitting is expected to be rather small because of the small ionicity of $Bi_2O_3$.[33]

As can be observed in Figure 2b, RS measurements at ambient pressure show four intense peaks at ∼90, ∼125, 313, and 465 cm$^{-1}$, and seven less intense peaks. The large number of Raman-active modes and the broadening of many of them make some modes hard to identify at room conditions because there are several close Raman peaks which overlap. In the next section we will show that other peaks can be observed because of the splitting of the Raman bands at high pressures. In particular, we have observed that the intense peaks at ∼90 and ∼125 cm$^{-1}$ are composed of pairs of modes at 89 and 94 cm$^{-1}$ and 124 and 127 cm$^{-1}$, respectively. Taking into account these considerations, it was possible to identify a total of 14 Raman-active modes at room conditions. The positions of these peaks are listed in Table 3 for comparison with the theoretical calculations and the results of previous works. As it can be observed in Table 3, our experimental and theoretical frequencies for the Raman-active modes at 1 atm are in good agreement and also agree with those already reported in the literature.[52]

SEM images of our $\beta$-$Bi_2O_3$ powders (Figure 2c) prove that they are composed of aggregated submicron particles with average size around 200 nm. In this respect, it is known that $\beta$-$Bi_2O_3$ is a metastable phase observed when the $\delta$ phase is cooled below 650 °C. The synthesis of metastable $\beta$-$Bi_2O_3$ as bulk material is based on the use of specific precursors, or as thin films, nanowires, nanoflakes, or nanospheres.[27,35,36,51,53−55] In our case, the fact that the samples have a submicrometric particle size promotes the stabilization of the $\beta$ phase at ambient conditions. To observe the elements present in the sample, EDX analysis was performed (see Figure 2d). No other elements, apart from Bi and O, were detected after a cleaning procedure in which C from the graphite film, which is needed to perform EDX measurements, and Be from the equipment window are removed. This indicates that no other element was used in the sample preparation to stabilize the $\beta$ phase. Note that the $\beta$ phase has been previously reported to be stabilized by intentionally substituting Bi with a lighter element[56] and by doping the $\alpha$ phase with $ZrO_2$.[57]

**4.2. XRD Measurements under Pressure.** Figure 3 shows the angle-dispersive XRD patterns of $\beta$-$Bi_2O_3$ with increasing pressure up to 27.2 GPa. We performed Rietveld refinement to the XRD patterns recorded up to 12 GPa using the tetragonal $P\bar{4}2_1c$ structure of $\beta$-$Bi_2O_3$. In this pressure range, all diffraction peaks shift to larger angles on increasing pressure, which is coherent with the decrease of interplanar distances with pressure, and some weak peaks disappear already at 2 GPa while a diffraction peak appears at ∼8.5° at 5.1 GPa (see asterisk in Figure 3). This peak is not due to $\beta$-$Bi_2O_3$, and we believe that it is related to some impurities unintentionally loaded inside the MDAC. At 16.8 GPa, the XRD pattern of $\beta$-$Bi_2O_3$ presents an important intensity loss and peak broadening which develops further on increasing pressure. Above 20 GPa, the XRD patterns show only broad bands besides the Cu diffraction peaks, indicating a possible amorphization of the sample. On decrease of pressure, the diffraction pattern obtained at 1.3 GPa shows peaks that correspond to the Bi−I structure (S.G. $R\bar{3}m$, no. 166) (see top of Figure 3),[58] suggesting that the sample undergo a decomposition process

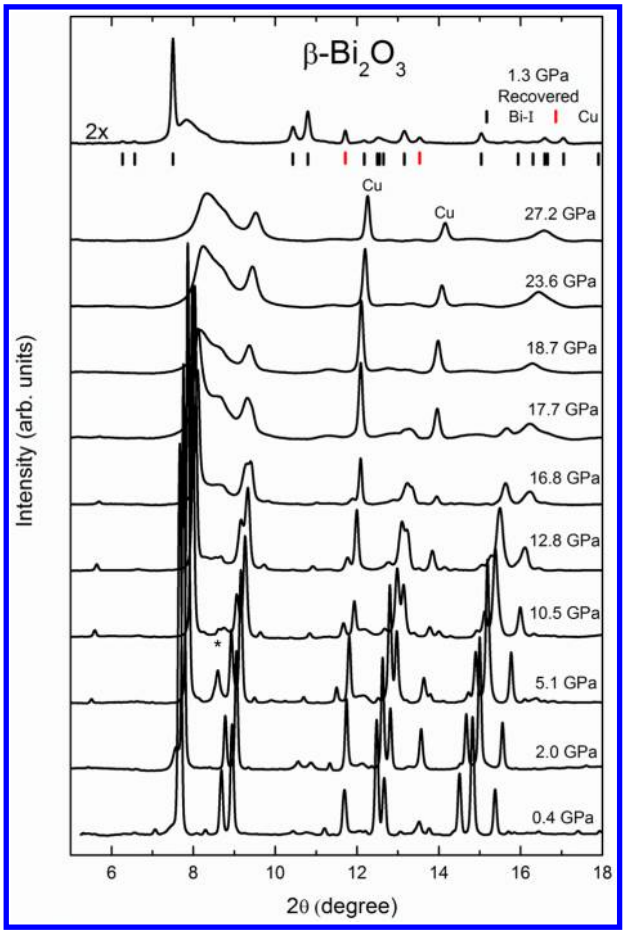


**Figure 3.** Angle-dispersive XRD of $\beta$-$Bi_2O_3$ measured at different pressures up to 27.2 GPa at room temperature. The top pattern corresponds to the recovered sample at 1.3 GPa after decompression from 27.2 GPa. Asterisk marks a peak not related to sample (see main text).


dx.doi.org/10.1021/jp507826j | J. Phys. Chem. C 2014, 118, 23189−23201

during downstroke which will receive further comment in the next section when discussing Raman spectra. The broad band observed in the pattern at 1.3 GPa on downstroke near 8° seems to correspond to the amorphous structure already observed at high pressure.

XRD data analysis allows us to estimate the pressure dependence of the lattice parameters ($a$,$c$) of $\beta$-$Bi_2O_3$ (see Figure 4a). The axial compressibility, defined as $k_x = -((1/x)(\partial x/\partial P))$, and obtained from a fit of experimental data to a modified Murnaghan EOS[59] are reported in Table 1 for $a$ and $c$ axes. We have estimated the axial compressibilities at zero pressure using data in three different pressure ranges: 0−12 GPa, 0−2 GPa, and 2−12 GPa. For the case of the $a$-axis, a strong decrease of the experimental axial compressibility at zero pressure ($\kappa_a$) is observed when comparing the value obtained in the range 0−2 GPa ($\kappa_a$ = 13.5 × $10^{-3}$ $GPa^{-1}$) with that obtained in the range 2−12 GPa ($\kappa_a$ = 4.1 × $10^{-3}$ $GPa^{-1}$). Our calculations are in agreement with this result. On the other hand, the evolution of the $c$-axis with pressure is not prone to vary, i.e., the experimental values of the axial compressibility for the $c$-axis ($\kappa_c$) obtained in the range 0−2 GPa and 2−12 GPa are very similar (see Table 1). The anomalous change in the compressibility of the $a$ lattice parameter is clearly exposed when we plot the evolution of the $c/a$ ratio with pressure (Figure 4b). Experimental $c/a$ shows a steep increase from 0.727 at 1 atm to 0.731 near 2 GPa and then a slow decrease to 0.723 at 12 GPa, which is rather well-reproduced by our theoretical calculations (Figure 4b). The strong decrease in compressibility of the $a$ lattice parameter and the change of sign in the slope of the $c/a$ ratio near 2 GPa clearly indicates the existence of an IPT from the $\beta$ phase toward a new phase (hereafter noted as $\beta'$) in $\beta$-$Bi_2O_3$.

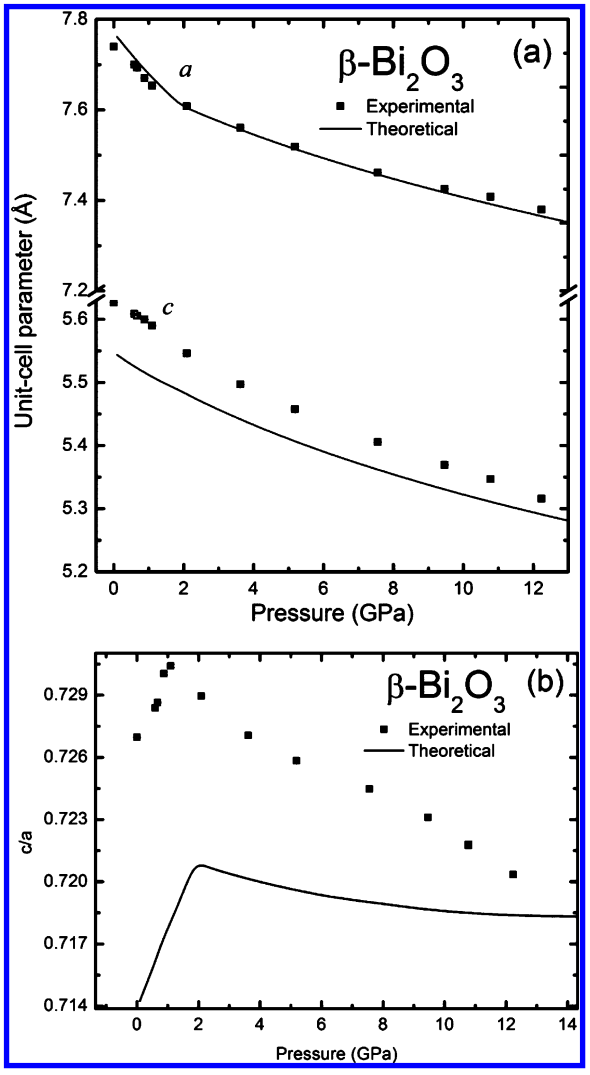


**Figure 4.** Experimental (symbols) and theoretical (lines) pressure dependence of (a) the lattice parameters $a$ and $c$ and (b) the $c/a$ ratio.

Figure 5 shows the experimental and theoretical pressure dependence of the unit-cell volume of $\beta$-$Bi_2O_3$ up to 12 GPa.

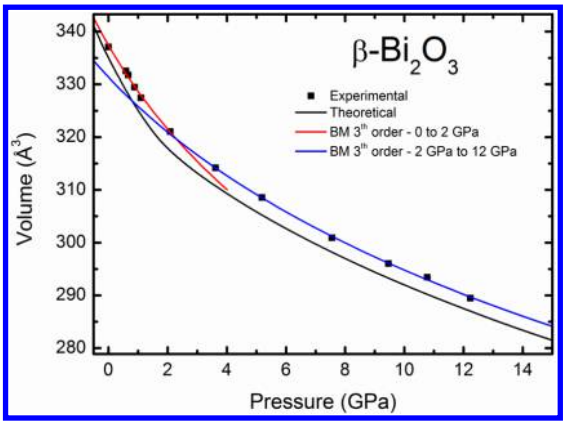


**Figure 5.** Unit-cell volume versus pressure for $\beta$-$Bi_2O_3$. Symbols represent experimental data, and solid lines the theoretical data. Red (blue) solid line corresponds to the third-order Birch−Murnaghan EOS fit to experimental data from 0 to 2 GPa (2 to 12 GPa).

The $P-V$ data are fitted using a second-order and third-order Birch−Murnaghan (BM) EOS to obtain the zero pressure volume ($V_0$), bulk modulus ($B_0$), and its pressure derivative ($B_0'$), which are summarized in Table 1 and compared with the values obtained from our theoretical calculations. As it can be observed in Table 1, the fit of all data using the third-order BM EOS leads to an unusually large value for $B_0'$ for both experimental and theoretical results. This large derivative ($B_0' > 10$) indicates a strong increase in the $B_0$ value of $\beta$-$Bi_2O_3$ with increasing pressure, especially above 2 GPa, and suggests a rather unusual compression of the $\beta$ phase. Following the previous results, it has more physical meaning to fit the $P-V$ data taking data points from two different pressure ranges: (i) 0−2 GPa ($\beta$ phase) and (ii) 2−12 GPa ($\beta'$ phase). The results of the EOS for both experimental and theoretical data fitted to second-order and third-order BM EOS in these two ranges are summarized in Table 1. We note that by fitting EOS to both experimental and theoretical data in two separated pressure ranges, we achieved more reasonable results for $B_0$ and $B_0'$. In the case of our experimental data, for $\beta$-$Bi_2O_3$ from 1 atm to 2 GPa, we get $B_0$ = 38(1) GPa when we constrain $B_0'$ to 4. A fit using a third-order BM EOS yields $B_0$ = 34(5) GPa and $B_0'$ = 8(5). For $\beta'$-$Bi_2O_3$ above 2 GPa, the material becomes rather more resistant to compression with $B_0$ = 77(2) GPa when we constrain $B_0'$ = 4, or $B_0$ = 55(17) GPa with $B_0'$ = 8(4) when data are fitted to a third-order BM EOS. It can be noted that when we separate the $P-V$ curve into two zones, the uncertainties in the determination of $B_0'$ from the experimental results are relatively high when compared to the theoretical results. This is related to the limited number of experimental points that we have in both pressure zones. Nevertheless, the


dx.doi.org/10.1021/jp507826j | J. Phys. Chem. C 2014, 118, 23189−23201

Table 1. EOS Parameters and Axial Compressibility at Zero Pressure of $\beta$-$Bi_2O_3$

| | $V_0$ (Å$^3$) | $B_0$ (GPa) | $B_0'$ | $\kappa_a$ ($\times 10^{-3}$ GPa$^{-1}$) | $\kappa_c$ ($\times 10^{-3}$ GPa$^{-1}$) |
|---|---|---|---|---|---|
| experimental (entire range) | 337.1(7) | 33(3) | 14(2) | 10.1(5) | 9.7(4) |
| theoretical (entire range) | 332.1(8) | 39.7(30) | 11.1(9) | 10.5(1) | 6.34(4) |
| experimental (up to 2 GPa) | 337.9(3) | 38(1) | 4.0 (fixed) | 13.5(5) | 6.2(1) |
| | 338.2(5) | 34(5) | 8(5) | | |
| theoretical (up to 2 GPa) | 334.8(2) | 32.5(5) | 4.0 (fixed) | 12.9(6) | 7.7(2) |
| | 335.0(1) | 29.6(10) | 7(1) | | |
| experimental (from 2 to 12 GPa) | 327(2) | 77(2) | 4.0 (fixed) | 4.1(1) | 5.8(2) |
| | 331(3) | 55(17) | 8(4) | | |
| theoretical (from 2 to 12 GPa) | 322.8(5) | 84(1) | 4.0 (fixed) | 4.88(7) | 6.28(6) |
| | 326(1) | 59.6(6) | 7.1(1) | | |

Table 2. Experimental and Theoretical Atomic Coordinates of Synthetic $\beta$-$Bi_2O_3$ at 1 atm and Theoretical Atomic Coordinates of $\beta'$-$Bi_2O_3$ at 2.3 GPa

| | | | 1 atm | | | 2.3 GPa | | |
|---|---|---|---|---|---|---|---|---|
| atom | site | | $x$ | $y$ | $z$ | $x$ | $y$ | $z$ |
| Bi | 8$e$ | theor. | 0.0213 | 0.257 | 0.231 | 0.000 | 0.252 | 0.221 |
| | | exptl. | 0.01902(14) | 0.25420(26) | 0.2378(4) | | | |
| O1 | 8$e$ | theor. | 0.289 | 0.313 | 0.034 | 0.297 | 0.297 | 0.000 |
| | | exptl. | 0.3006(25) | 0.3149(23) | 0.014(4) | | | |
| O2 | 4$d$ | theor. | 0.000 | 0.500 | 0.405 | 0.000 | 0.500 | 0.397 |
| | | exptl. | 0.000 | 0.500 | 0.379(4) | | | |

values of $B_0'$ obtained from the experiment when we have divided all data into two pressure ranges presents more consistent values ($B_0' < 10$), despite being relatively high when compared to ionic−covalent solids, and are in good agreement with the theoretical results (see Table 1).

It is noteworthy the higher compressibility of tetragonal $\beta$-$Bi_2O_3$ ($B_0$ = 38(1) GPa) than monoclinic $\alpha$-$Bi_2O_3$ ($B_0$ = 79.2(3) GPa[33]). The bulk modulus of $\beta$-$Bi_2O_3$ is comparable to those of molecular solids like senarmontite, the most common phase of $Sb_2O_3$,[60] and likely to that of arsenolite, the most common phase of $As_2O_3$. The presence of a second-order IPT in tetragonal $\beta$-$Bi_2O_3$, i.e., a phase transition without any change in the symmetry of the crystalline lattice and no discontinuity in the volume,[61] is similar to those already observed in $Bi_2S_3$,[50] $Sb_2O_3$,[60] and $BiMn_2O_5$.[62]

Rietveld refinements performed at 0.6 GPa yield residuals of $R_p$ = 0.7% and $R_{wp}$ = 1.1%, while those performed at 12 GPa yielded $R_p$ = 1.8% and $R_{wp}$ = 2.7%. In the $\beta$ phase, one Bi and one O occupy 8$e$ ($x$,$y$,$z$) Wyckoff sites while the other O occupies a 4$d$ (0,1/2,$z$) Wyckoff site, as previously discussed. Because O has an X-ray scattering cross section smaller than that of Bi, it is difficult to obtain accurately the four atomic coordinates corresponding to the two different oxygen atoms by Rietveld refinement of the XRD patterns at high pressures. Therefore, the atomic coordinates of the oxygen atoms were refined just at 1 atm and constrained in the following refinements up to 2 GPa. On the other hand, the Bi fractional coordinates and unit-cell parameters were refined up to 2 GPa. From 2 GPa, we observed a significant change in the evolution of the lattice parameters with pressure, but we did not obtain coherent values in the refinement of the Bi position. For this reason, from 2 to 12 GPa we constrained the values of atomic position obtained by our theoretical calculations at 2.3 GPa for the Bi and the two O. The atomic coordinates obtained by the Rietveld refinement at 1 atm and the theoretical ones at 1 atm and at 2.3 GPa (to perform the refinements in the $\beta'$ phase) are presented in Table 2. The values obtained at 1 atm are in good agreement with the results obtained by neutron diffraction[51] and with the values obtained by our theoretical calculations.

Figure 6 shows the calculated evolution of the atomic coordinates of Bi (8$e$), O1 (8$e$), and O2 (4$d$) atoms with increasing pressure. The clear change in the evolution of the atomic coordinates of all atoms near 2 GPa is worth noting. For Bi, the $x_{Bi}$ coordinate, initially at 0.021, decreases sharply to zero at 2 GPa and becomes independent of pressure above 2 GPa (see Figure 6a). The evolution of the $y_{Bi}$ and $z_{Bi}$ position with pressure, initially near 0.26 and 0.23, respectively, also present a decrease (but less intense) up to 2 GPa and for the case of $y_{Bi}$ remains almost constant above this pressure. In this respect, we want to stress that the refinement of the experimental Bi position performed up to 2 GPa matches very well with our theoretical results (Figure 6a). For O1, the $z_{O1}$ coordinate decreases from 0.034 to zero at 2 GPa and becomes independent of pressure above 2 GPa, while the $x_{O1}$ and $y_{O1}$ coordinates tend to a single value above 2 GPa (Figure 6b). Finally, the $z_{O2}$ coordinate shows a change in the slope at 2 GPa (Figure 6c). Note that the experimental and theoretical $z_{O2}$ coordinate at 1 atm shows a deviation slightly larger than that of other coordinates; however, our experimental value (0.38) is not very different from that previously reported from neutron diffraction experiments (0.39).[51] The above commented changes clearly show that some of the Bi and O coordinates tend to fixed values at 2 GPa, indicating an increase of the symmetry of all occupied Wyckoff sites and, consequently, of the compound above 2 GPa.

The increase of symmetry on going from $\beta$-$Bi_2O_3$ to $\beta'$-$Bi_2O_3$ can be clearly seen in Figure 7a, which shows the theoretical evolution of the Bi−O distances in the $BiO_6$ polyhedron. At 1 atm, the $BiO_6$ polyhedron is highly asymmetric with six different Bi−O distances, which suggests the existence of a localized and very active LEP. When pressure is increased, the Bi−O1(2) distance decreases and the Bi−O1(1) distance increases so that these two distances coincide at 2 GPa, having both a similar decrease with pressure above 2 GPa (Figure 7a).


dx.doi.org/10.1021/jp507826j | J. Phys. Chem. C 2014, 118, 23189−23201

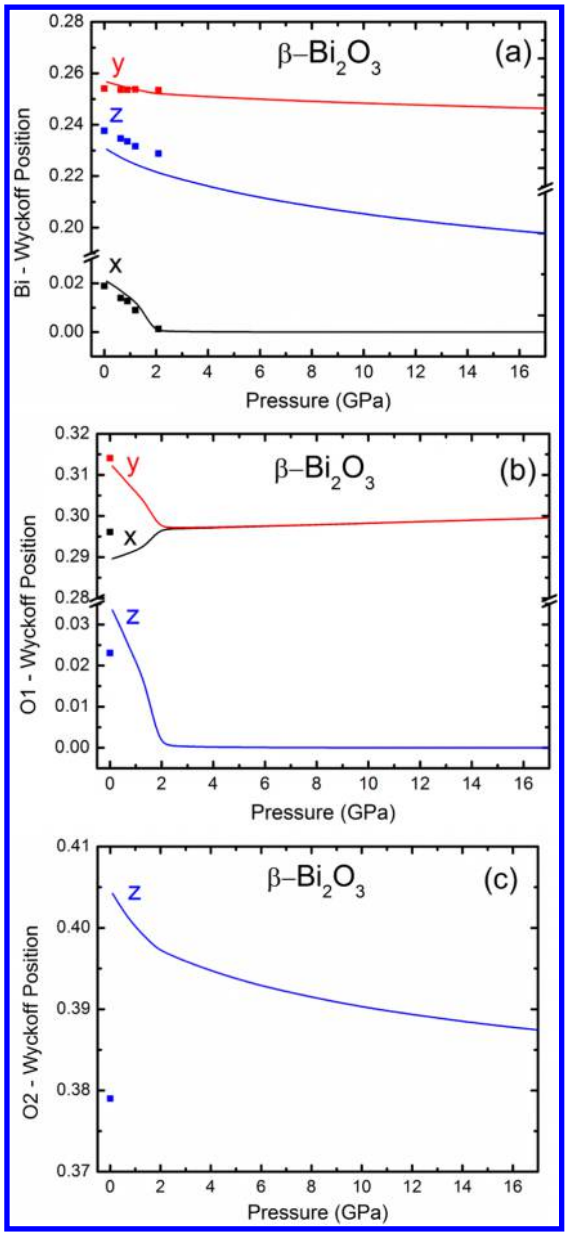


**Figure 6.** Experimental (squares) and theoretical (solid lines) evolution of the (a) Bi, (b) O1, and (c) O2 atomic coordinates of the different Wyckoff positions in $\beta$-$Bi_2O_3$ as a function of pressure.

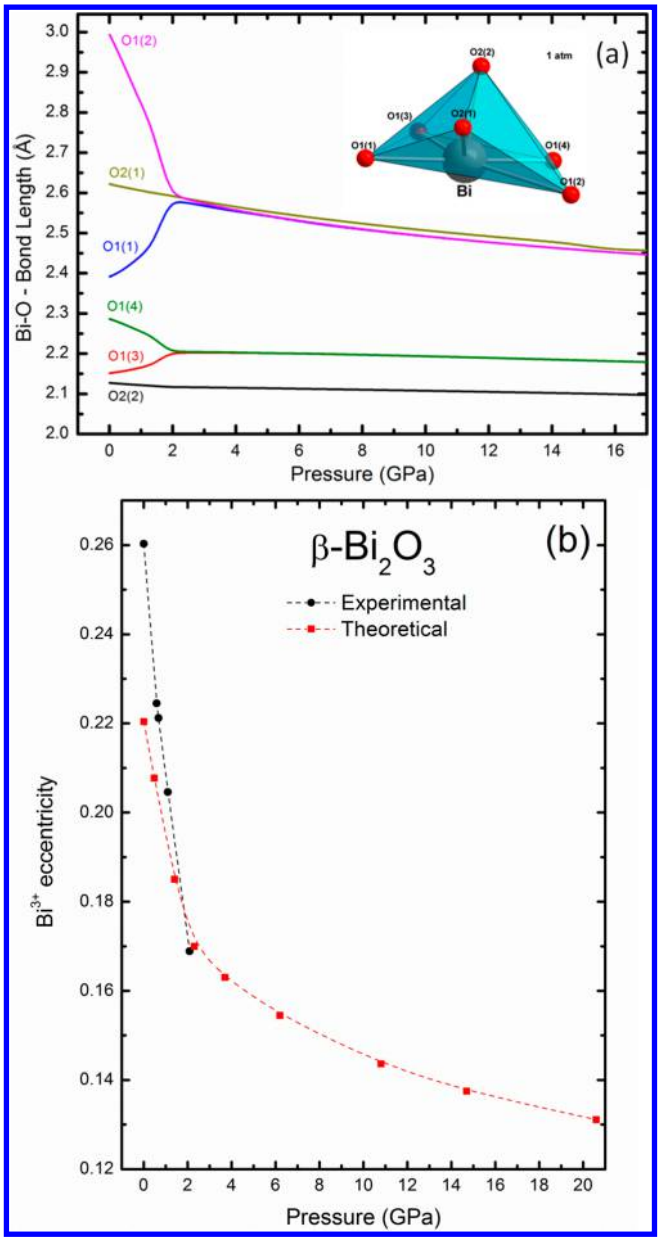


**Figure 7.** (a) Theoretical evolution of the Bi–O bond lengths with pressure. (b) Experimental (black) and theoretical (red) evolution of the Bi eccentricity with pressure.

A similar behavior can also be observed between the Bi–O1(4) and Bi–O1(3) distances (see Figure 7a). On the other hand, the Bi–O2 distances do not present such a drastic behavior with pressure: the Bi–O2(1) distance presents a smooth decrease and the Bi–O2(2) distance presents an almost insignificant decrease (see Figure 7a). In summary, the $BiO_6$ polyhedron above 2 GPa exhibits basically only three different Bi–O distances, two of which do not change significantly with the pressure increase (see Figure 7a). These results indicate that compression up to 2 GPa induces a relatively fast regularization of the polyhedron which forms the $\beta$-$Bi_2O_3$ structure while the variation is very smooth above 2 GPa, i.e., the pressure dependence of the Bi–O distances again shows the increase of symmetry of the tetragonal structure of $\beta$-$Bi_2O_3$ on increasing pressure.

The key to understanding the compression mechanism and the IPT in $\beta$-$Bi_2O_3$ resides in the understanding of the LEP activity of $Bi^{3+}$ ion, which is one major cause of the distortion in coordination polyhedral of LEP-bearing compounds.[31,63] Hence, studying the evolution of the polyhedral distortion with pressure can give us important information about the LEP activity.[63] The polyhedral distortion of the $Bi^{3+}$ environment can be monitored by the displacement of the cation relative to the centroid of the coordination polyhedron, the centroid being the point which comes closest to the condition of being equidistant to all the coordinated ligands. The displacement of the cation relative to this point divided by the average distance of the cation to ligands is called the eccentricity.[63,64] The eccentricity is an important parameter to estimate the stereochemical LEP activity (when eccentricity becomes equal to zero, the LEP ceases to exist). The pressure dependence of Bi eccentricity in $\beta$-$Bi_2O_3$ is plotted in Figure 7b. It can be observed that the experimental eccentricity of $Bi^{3+}$ in $\beta$-$Bi_2O_3$ obtained at 1 atm (0.26) is in good agreement with our


dx.doi.org/10.1021/jp507826j | J. Phys. Chem. C 2014, 118, 23189–23201

theoretical calculation (0.22) and also agrees with the eccentricity of $Bi^{3+}$ in $Bi_2Ga_4O_9$ (0.28) at 1 atm.[63] For the sake of comparison, we have also calculated the eccentricity of the two unequivalent $Bi^{3+}$ atoms in $\alpha$-$Bi_2O_3$ at 1 atm. Both eccentricities show to be lower (0.16 for Bi1 and 0.17 for Bi2) than that of $Bi^{3+}$ in $\beta$-$Bi_2O_3$. The $Bi^{3+}$ eccentricity in the $\beta$-$Bi_2O_3$ also is higher than that in the $Bi_2S_3$ (0.14 for Bi1 and 0.16 for Bi2),[66] which also shows a pressure-induced IPT,[50] $PbBi_2S_4$ (between 0.08 and 0.12),[67] and $Pb_3Bi_2S_6$ (between 0.04 and 0.10),[68] thus suggesting that the value of cation eccentricity depends not only on the structure but also on the anion.

Regarding the pressure dependence of experimental (theoretical) eccentricity of $Bi^{3+}$ in $\beta$-$Bi_2O_3$, it shows a steep decrease from 0.26 (0.22) at 1 atm to 0.17 at 2 GPa. Our calculations show a smooth decrease above 2 GPa from 0.17 until 0.13 at 12 GPa. Experimental eccentricity could not be calculated at pressures higher than 2 GPa because we did not obtain coherent values in the refinement of the atomic positions above that pressure, as previously discussed. The notable decrease of the pressure coefficient of calculated eccentricity (Figure 7b) is consistent with the more regular $BiO_6$ polyhedron in the $\beta'$ phase (above 2 GPa) than in the $\beta$ phase (below 2 GPa). Extrapolations of the tendencies found in Figure 7b show that eccentricity will become zero at ~10 GPa in the $\beta$ phase and at ~90 GPa in the $\beta'$ phase. These results clearly indicate that the LEP remains active in the $\beta'$ phase after the second-order IPT has taken place in $\beta$-$Bi_2O_3$. This result indicates that the LEP activity decreases but does not disappear. A pronounced LEP activity at high pressure also occurs in a number of other compounds, such as HP-$Bi_2O_3$,[31] $Bi_2Ga_4O_9$,[63] $Bi_2S_3$, $Cu_4Bi_5S_{10}$,[65,66] $PbBi_2S_4$,[67] $Pb_6Bi_2S_9$,[69] and $Bi_2Fe_4O_9$.[70] In summary, it can be concluded that despite the fact that the role of the cation LEP in producing distorted polyhedra and in pressure-induced phase transitions is still a matter of debate,[65,71] the reported studies seem to suggest that LEP activity decreases with the increase of anion mass and with the increase of pressure. The reduction of the LEP activity results in a more centered position for the cation in the polyhedral units, and in particular, it can lead to new isostructural phases at high pressures, as occurs in $\beta$-$Bi_2O_3$, $Bi_2S_3$, and $\alpha$-$Sb_2O_3$.

### 4.3. Raman Scattering Measurements under Pressure.

Figure 8 shows the Raman spectra of $\beta$-$Bi_2O_3$ at selected pressures up to 27 GPa. The large number of Raman-active modes and the broadening of many of them make some modes hard to identify at room conditions because there are several close Raman peaks which overlap. This is similar to the case of $\alpha$-$Bi_2O_3$ already discussed in the literature.[34,72] Three weak peaks at 30, 161, and 197 $cm^{-1}$ disappear with increasing pressure before reaching 2 GPa. This result supports the analysis made in the previous section. However, the pressure increase allows a clear observation of two new peaks that were overlapped with more intense peaks, near 90 and 125 $cm^{-1}$ at 1 atm, and another weak peak that was detected at ~500 $cm^{-1}$ in the $\beta'$ phase above 2 GPa. Above 15 GPa, some new peaks develop while peaks of $\beta'$ phase have an important intensity decrease. This decrease is severe above 19 GPa, and the appearance of six new weak peaks near 100, 130, 220, 420, 470, and 500 $cm^{-1}$ at 19.1 GPa and near to 120 $cm^{-1}$ at 20.3 GPa suggest the onset of a phase transition to a new phase, hereafter noted $\chi$ phase (see Figure 8). At 21.9 GPa, the Raman peaks of the $\beta'$ phase completely lose their shapes and intensities and only broad bands are observed, which is consistent with a partial amorphization of the material as observed by XRD

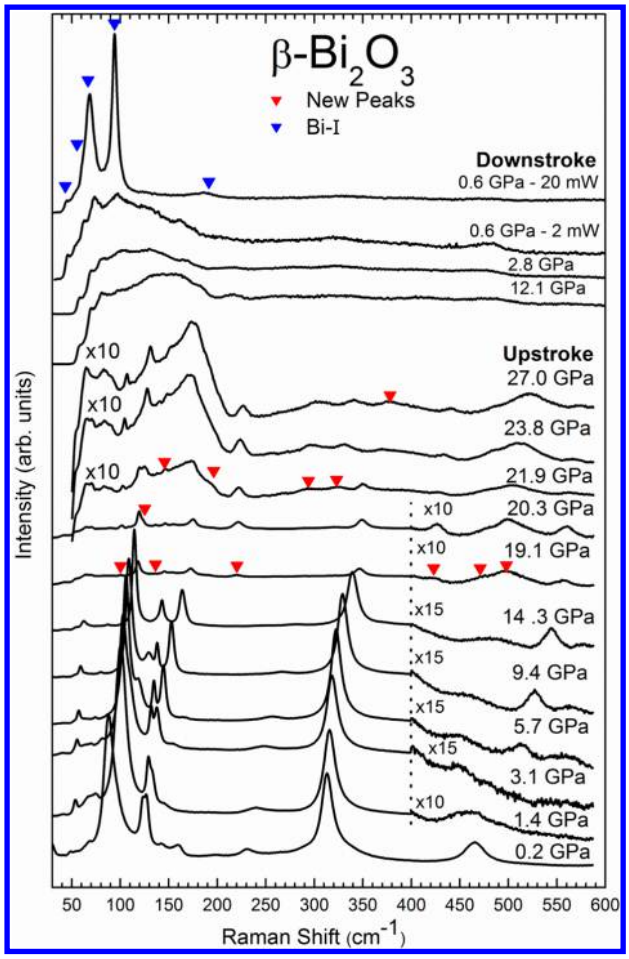


**Figure 8.** Room-temperature Raman spectra of $\beta$-$Bi_2O_3$ at selected pressures up to 27 GPa. The top patterns correspond to the recovered sample after decompression from 27 GPa.

measurements. At 21.9 GPa, new peaks appear near to 150, 200, 295, and 320 $cm^{-1}$, which could correspond to the $\chi$ phase; however, amorphization prevented the identification of this new phase from our XRD measurements. All the new peaks developed above 15 GPa and at 21.9 GPa remain overlapped with the amorphous bands up to 27 GPa. At this pressure, it is possible to observe another small band near 380 $cm^{-1}$ (Figure 8). When the pressure is decreased, we observed a RS spectrum consisting mainly of broad bands coming from the amorphous phase. However, when pressure is decreased below 2 GPa, the RS spectrum exhibits new peaks which further develop under strong laser irradiation (see two top spectra in Figure 8), and these RS spectra are completely different than that of the original sample. We have checked that this RS spectrum corresponds to the pure Bi–I structure;[73] therefore, our RS measurements agree with our XRD data and reinforce the idea that $\beta$-$Bi_2O_3$ exhibits a decomposition on decreasing pressure from 27 GPa.

Regarding the dissociation of the sample, we must stress that the new peaks observed above 15 GPa cannot be associated with the high-pressure cubic bcc structure of Bi[58] because this phase has no Raman-active modes. Furthermore, they cannot be attributed to solid $\varepsilon$-$O_2$ because none of the bands of this phase,[74,75] including the vibron mode above 1600 $cm^{-1}$, has been observed in $\beta$-$Bi_2O_3$ above 15 GPa. Therefore, at present we do not know the origin of the new Raman bands that appear


dx.doi.org/10.1021/jp507826j | J. Phys. Chem. C 2014, 118, 23189–23201

above 15 GPa and which we tentatively attribute to the $\chi$ phase of $Bi_2O_3$; however, we can conclude that on upstroke there is an amorphization and not a dissociation of $\beta$-$Bi_2O_3$.

Figure 9 shows the experimental (symbols) and theoretical (solid lines) Raman-mode frequencies of $\beta$-$Bi_2O_3$ as a function of pressure up to 27 GPa. For the sake of clarity, a low-frequency region (below 250 $cm^{-1}$) and a high-frequency region (above 250 $cm^{-1}$) are plotted in panels a and b of Figure 9, respectively. Figure 9a,b can be divided into four pressure regions: (i) from 1 atm to 2 GPa, region of stability of the $\beta$ phase; (ii) from 2 to 15 GPa, region of stability of the $\beta'$ phase; (iii) from 15 to 22 GPa, region where some peaks of the $\beta'$ phase start to disappear and new peaks appear, thus indicating the beginning of a phase transition to the $\chi$ phase; and (iv) above 22 GPa, only the peaks of the $\chi$ phase are observed together with signatures of pressure-induced amorphization.

In the first region from 1 atm to 2 GPa of Figure 9a,b, the pressure dependence of 14 Raman-active modes of $\beta$-$Bi_2O_3$ observed at ambient pressure and two new peaks that appear with pressure increase are shown. Table 3 summarizes the zero-pressure experimental and theoretical frequencies and their pressure coefficients for the Raman-active modes as well as their symmetries. Results previously reported at 1 atm on powder samples[52] are also shown in Table 3 for comparison. Most of these Raman modes can be followed in the second region from 2 to 15 GPa because those modes correspond also to Raman-active modes in $\beta'$-$Bi_2O_3$. At 2 GPa there are considerable changes in the pressure coefficients of some Raman-active modes. Some of them have been experimentally measured. In particular, the most notable is the change of the pressure coefficient of the $A_1$ mode initially at 465 $cm^{-1}$. This soft mode exhibits a negative pressure coefficient (−7.6 $cm^{-1}$/GPa) up to 2 GPa, and above this pressure, the pressure coefficient is positive (2.8 $cm^{-1}$/GPa). All these changes reinforce the evidence for the pressure-induced IPT taking place near 2 GPa in $\beta$-$Bi_2O_3$. For this reason, the pressure coefficients of all Raman-active modes were calculated in two pressure ranges: below 2 GPa ($\beta$ phase) and above 2 GPa ($\beta'$ phase). The good agreement between our experimental and theoretical frequencies and pressure coefficients (see Figure 9 and Table 3) has allowed us to make a tentative assignment of the symmetry of the observed Raman peaks. It must be stressed that the symmetry assignment to experimental Raman peaks is not easy because many peaks overlap due to the large number of Raman modes, as indeed evidenced by our theoretical calculations.

Concerning the pressure dependence of the Raman-active modes of $\beta$-$Bi_2O_3$, our calculations predict the presence of several soft modes and that some of them undergo anticrossings between 1 and 2 GPa (see Figure 9). The presence of a number of pressure-induced phonon anticrossings at $\Gamma$ has been recently reported in $\alpha$-$Bi_2O_3$.[34] The most striking feature of the Raman-active modes of $\beta$-$Bi_2O_3$ is the presence of an optic soft $A_1$ mode near 50 $cm^{-1}$ at 1 atm whose frequency goes to zero near 2 GPa. This soft mode clearly shows a square root pressure dependence before and after 2 GPa, i.e., it can be fitted to $\omega = A(P_T - P)^{1/2}$ below $P_T$ = 2 GPa and to $\omega = B(P - P_T)^{1/2}$ above $P_T$ (see Figure 10a), where $P_T$ is the transition pressure and $A$ (∼35 $cm^{-1}\cdot GPa^{-1/2}$) and $B$ (∼17 $cm^{-1}\cdot GPa^{-1/2}$) are constants. According to the Landau theory of phase transitions, this soft mode behavior is usually related to a displacive second-order phase transition;[76,77] therefore, this result confirms the second-order nature of the pressure-induced

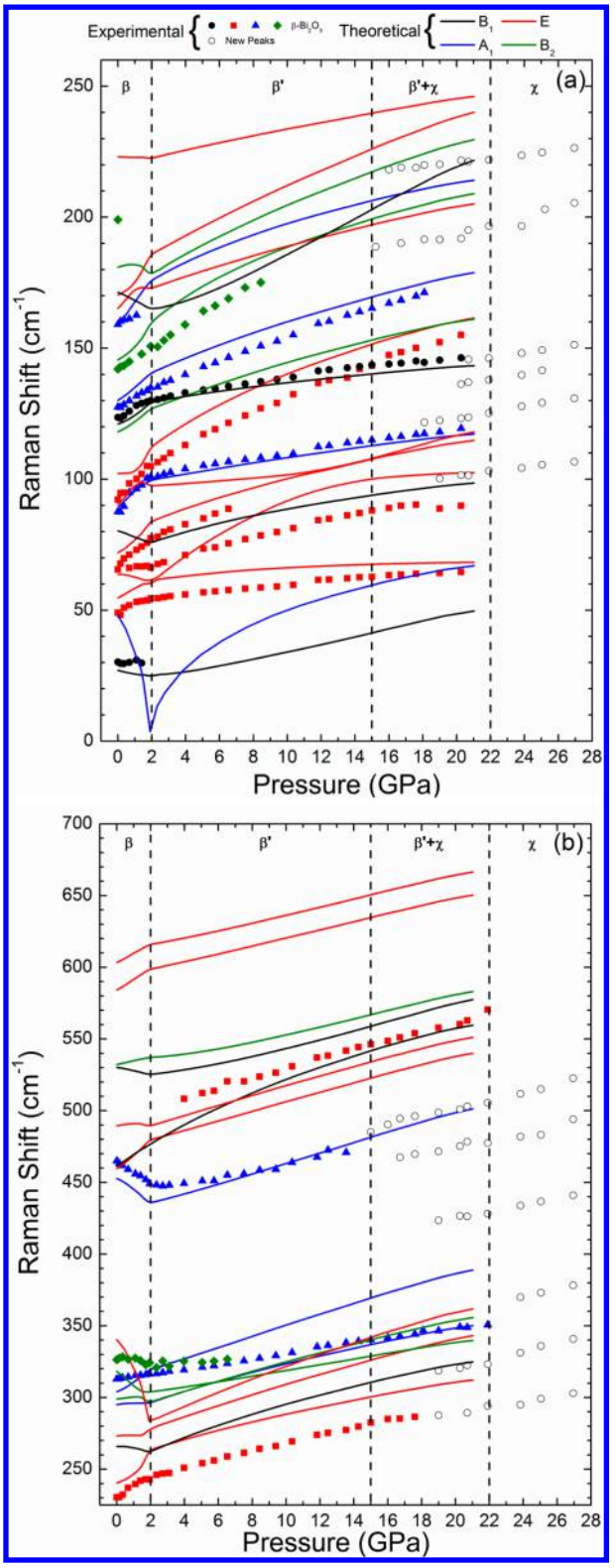


**Figure 9.** Experimental (symbols) and theoretical (lines) pressure dependence of the Raman-active modes of $\beta$-$Bi_2O_3$: (a) from 0 to 250 $cm^{-1}$ and (b) from 230 to 700 $cm^{-1}$. Different colors represent Raman-active modes of different symmetries.

IPT in $\beta$-$Bi_2O_3$. Curiously, the square root pressure dependence is also observed in other soft modes of $\beta$-$Bi_2O_3$ (see Figure 10a), thus suggesting that the soft low-frequency $A_1$ mode is coupled to other higher-frequency Raman-active soft


dx.doi.org/10.1021/jp507826j | J. Phys. Chem. C 2014, 118, 23189−23201

Table 3. Experimental and Theoretical Raman Mode Frequencies and Pressure Coefficients of $\beta$-$Bi_2O_3$ Obtained by Fitting the Equation $\omega(P) = \omega_0 + a \cdot P$ Compared with Those Obtained by Pérez-Salazar et al.[52] at Ambient Conditions[a]

| | experimental | | | theoretical | | | ref 52 |
|---|---|---|---|---|---|---|---|
| symmetry | $\omega_0$ ($cm^{-1}$) | $\alpha$ ($cm^{-1}$/GPa) 0–2 GPa | $\alpha$ ($cm^{-1}$/GPa) from 2 GPa | $\omega_0$ ($cm^{-1}$) | $\alpha$ ($cm^{-1}$/GPa) 0–2 GPa | $\alpha$ ($cm^{-1}$/GPa) from 2 GPa | $\omega_0$ ($cm^{-1}$) |
| $B_1$ | 30 | 0.29 | | 27.05 | −1.29 | 1.38 | |
| $A_1$ | | | | 48.04 | −22.0 | 2.43 | |
| E | 48 | 2.96 | 0.53 | 54.64 | 2.68 | 0.30 | |
| E | 66 | 5.45 | 2.72 | 63.68 | 0.42 | 2.05 | 69 |
| E | | 0.23 | 1.51 | 71.95 | 5.03 | 1.54 | |
| $B_1$ | | | | 80.26 | −0.98 | 1.14 | |
| $A_1$ | 89 | 7.32 | 0.97 | 89.20 | 5.92 | 0.93 | |
| E | 94 | 6.56 | 2.71 | 90.33 | 6.31 | 1.11 | 93 |
| E | | | | 102.14 | 5.02 | 2.47 | |
| $B_2$ | | | | 118.09 | 3.90 | 1.74 | |
| $B_1$ | 124 | 3.72 | 0.87 | 121.06 | 3.33 | 0.69 | |
| $A_1$ | 127 | 4.01 | 2.23 | 130.16 | 4.60 | 1.94 | 128 |
| $B_2$ | 142 | 4.38 | 4.06 | 145.57 | 6.70 | 2.20 | |
| $A_1$ | | | | 158.98 | 8.74 | 1.84 | |
| E | 161 | 2.94 | | 165.15 | 3.43 | 1.65 | |
| E | | | | 170.26 | 6.65 | 2.81 | |
| $B_1$ | | | | 171.33 | −1.98 | 3.32 | |
| $B_2$ | 197[b] | | | 180.93 | 0.17 | 2.60 | |
| E | | | | 223.00 | 0.29 | 1.21 | |
| E | 231 | 7.22 | 2.76 | 240.34 | 9.42 | 2.46 | |
| $B_1$ | | | | 265.79 | 0.18 | 3.14 | |
| E | | | | 273.20 | 3.04 | 3.38 | |
| $A_1$ | 313 | 1.84 | 1.84 | 294.98 | 1.67 | 2.72 | 317 |
| $B_2$ | 326 | −2.20 | 1.80 | 298.92 | −0.70 | 3.60 | |
| $A_1$ | | | | 304.02 | 6.67 | 3.71 | |
| $B_2$ | | | | 318.10 | −4.65 | 1.95 | |
| E | | | | 340.38 | −19.04 | 4.12 | |
| $A_1$ | 465 | −7.61 | 3.17 | 452.73 | −5.29 | 3.57 | 461 |
| E | | | | 459.67 | 8.15 | 3.22 | |
| $B_1$ | | | | 461.41 | 7.53 | 4.12 | |
| E | 497[c] | | 3.27 | 489.46 | 0.99 | 3.26 | |
| $B_1$ | | | | 530.19 | −1.38 | 2.95 | |
| $B_2$ | | | | 532.16 | 2.01 | 2.7 | |
| E | | | | 584.20 | 5.9 | 2.8 | |
| E | | | | 603.34 | 5.1 | 2.8 | |

[a]To perform the fit, data were separated into two regions: from 1 atm to 2 GPa ($\beta$ phase) and from 2 GPa onwards ($\beta'$ phase). [b]The peak disappears with pressure increase. [c]Peak not observed at 1 atm.

modes and that there is more than one soft mode involved in the mechanism of the transformation. This hypothesis is supported by the complex symmetry of the $BiO_6$ polyhedron in $\beta$-$Bi_2O_3$ and the impossibility of distinguishing between low-frequency and high-frequency regions of external and internal modes of the $BiO_6$ polyhedron because they are very much coupled, as in $\alpha$-$Bi_2O_3$.[34]

To further investigate which of the soft modes are indeed related to the mechanism causing the $\beta$–$\beta'$ IPT near 2 GPa, we have evaluated the shift of the atoms caused by these vibrational modes and the evolution of the experimental intensities of these modes. From the nine soft modes predicted by our theoretical lattice dynamics calculations, only one was observed experimentally, i.e., the $A_1$ mode at 465 $cm^{-1}$. As can be observed in Figures 8 and 10b, the intensity of this mode decreases significantly with the increase of pressure up to 2 GPa. Above this pressure, it remains constant despite the low intensity (Figure 8). We think that the decrease in intensity is due to the change in polarizability of the lattice due to the IPT as a consequence of the increase in the symmetry of the $BiO_6$ polyhedron in the $\beta'$ phase. Furthermore, the decrease in intensity of the $A_1$ mode at 465 $cm^{-1}$ with pressure mimics the pressure dependence of the $Bi^{3+}$ eccentricity, thus giving support to the existence of the pressure-induced IPT near 2 GPa. A systematic analysis of the eigenvectors of the nine soft modes indicates that all of them contribute partially to the atomic displacements of Bi, O1, and O2 characteristic of the $\beta$ to $\beta'$ IPT and shown in Figure 6. In particular, the $A_1$ mode whose frequency falls to zero at 2 GPa is related to a significant displacement of the Bi and the O1 atoms in the $x$ and $z$ direction, respectively, agreeing with the results plotted in Figure 6. On the other hand, the $A_1$ mode initially at 453 $cm^{-1}$ and observed experimentally has a strong displacement of the O1 atom in the $y$ and $z$ direction, which also is in good agreement with results plotted in Figure 6. In summary, we propose that the IPT observed at 2 GPa is a second-order phase transition related to a displacive movement of the atoms in which all the nine soft modes show a partial contribution.


dx.doi.org/10.1021/jp507826j | J. Phys. Chem. C 2014, 118, 23189–23201

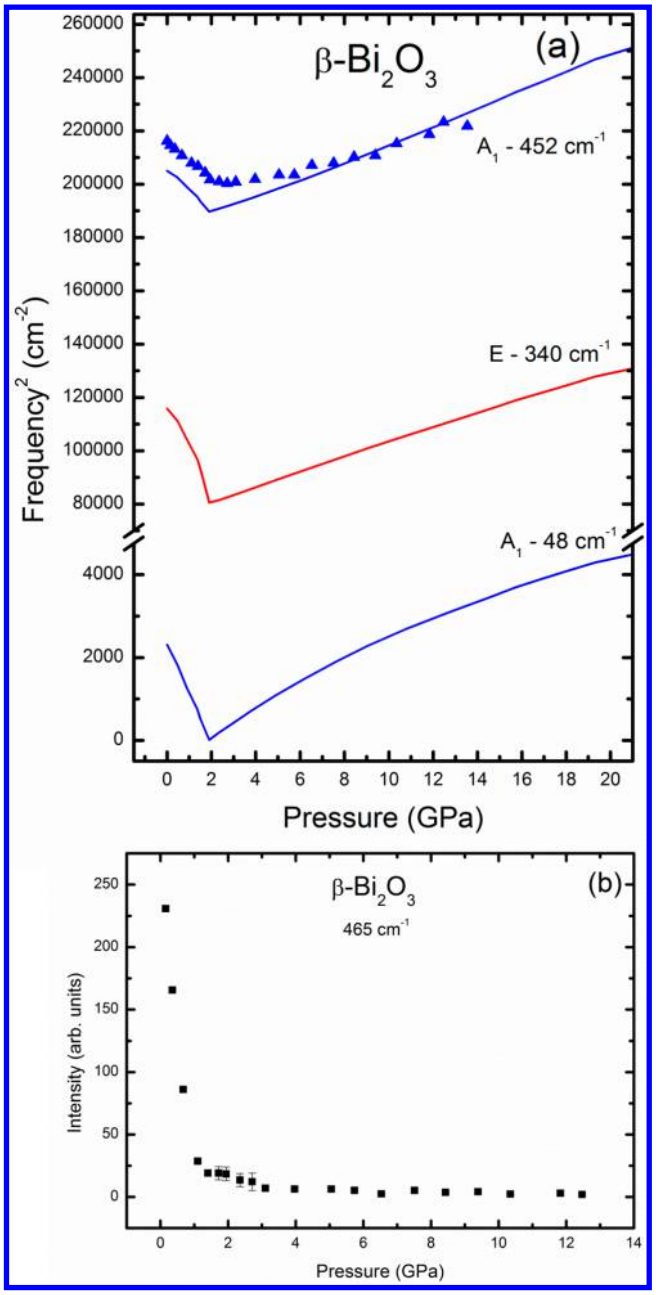


**Figure 10.** (a) Pressure dependence of the experimental (symbols) and theoretical (lines) square frequency of two $A_1$ and one E soft modes. (b) Pressure dependence of the experimental absolute intensity of the 465 $cm^{-1}$ peak at 1 atm (calculations locate it at 452 $cm^{-1}$) and attributed to the high-frequency $A_1$ mode.

## 5. CONCLUSIONS

Our joint high-pressure experimental and theoretical study of the structural and vibrational properties of synthetic $\beta$-$Bi_2O_3$ at room temperature shows evidence that this compound undergoes a second-order isostructural phase transition ($\beta$ to $\beta'$) near 2 GPa. The experimental and theoretical equations of state of the two structures ($\beta$ and $\beta'$) as well as the pressure dependence of their Raman-active modes have been reported. Our theoretical lattice dynamics calculations suggest that the isostructural transition is of second-order type and is driven by nine soft optical vibrational modes that displace the atoms in the $\beta'$ phase to a position that is more stable and regular than that in the $\beta$ phase.

In the $\beta'$ phase, the $Bi^{3+}$ environment becomes more regular than in the $\beta$ phase in good agreement with the decrease of the lone electron pair activity of $Bi^{3+}$ with increasing pressure, as indicated by the Bi eccentricity. Interestingly, our results indicate that the isostructural phase transition is not a consequence of the vanishing of the lone electron pair activity, and care must be taken when eccentricity values obtained at low pressures are extrapolated to high pressures. The extrapolation of the pressure dependence of the eccentricity below 2 GPa at higher pressures could lead to the conclusion that the electron pair activity vanishes at 10 GPa; however, our calculation of the eccentricity values in the $\beta'$ phase above 2 GPa allows us to predict that the vanishing of the lone electron pair activity does not occur at least up to 90 GPa.

Our X-ray diffraction and Raman scattering measurements indicate a partial amorphization of the structure above 20 and 21.9 GPa, respectively. However, Raman scattering measurements present some weak peaks above 15 GPa, probably related to a new unknown phase which remains up to 27 GPa. On decreasing pressure from 27 GPa, both measurements provide evidence of the decomposition of the sample below 2 GPa, which is stimulated by local laser heating.

## AUTHOR INFORMATION

### Corresponding Author

*E-mail: andeje@upv.es.

### Notes

The authors declare no competing financial interest.

## ACKNOWLEDGMENTS

Financial support from the Spanish Consolider Ingenio 2010 Program (MALTA Project CSD2007-00045) is acknowledged. This work was also supported by Brazilian Conselho Nacional de Desenvolvimento Científico e Tecnológico (CNPq) under Project 201050/2012-9, Spanish MICINN under Projects MAT2010-21270-C04-01/03/04 and MAT2013-46649-C4-2/3/4-P, Spanish MINECO under Project CTQ2012-36253-C03-02, and from Vicerrectorado de Investigación de la Universitat Politècnica de València under Projects UPV2011-0914 PAID-05-11 and UPV2011-0966 PAID-06-11. Supercomputer time has been provided by the Red Española de Supercomputación (RES) and the MALTA cluster. J.A.S. acknowledges Juan de la Cierva fellowship program for financial support.

## REFERENCES

(1) Ai, Z.; Huang, Y.; Lee, S.; Zhang, L. Monoclinic $\alpha$-$Bi_2O_3$ Photocatalyst for Efficient Removal of Gaseous NO and HCHO under Visible Light Irradiation. *J. Alloys Compd.* **2011**, *509*, 2044−2049.

(2) Bessekhouad, Y.; Robert, D.; Weber, J. V. Photocatalytic Activity of $Cu_2O/TiO_2$, $Bi_2O_3/TiO_2$ and $ZnMn_2O_4/TiO_2$ Heterojunctions. *Catal. Today* **2005**, *101*, 315−321.

(3) Cabot, A.; Marsal, A.; Arbiol, J.; Morante, J. R. $Bi_2O_3$ as a Selective Sensing Material for NO Detection. *Sens. Actuators, B* **2004**, *99*, 74−89.

(4) Zhou, L.; Wang, W. Z.; Xu, H. L.; Sun, S. M.; Shang, M. $Bi_2O_3$ Hierarchical Nanostructures: Controllable Synthesis, Growth Mechanism, and their Application in Photocatalysis. *Chem.—Eur. J.* **2009**, *15*, 1776−1782.

(5) Zheng, F. L.; Li, G. R.; Ou, Y. N.; Wang, Z. L.; Su, C. Y.; Tong, Y. X. Synthesis of Hierarchical Rippled $Bi_2O_3$ Nanobelts for Supercapacitor Applications. *Chem. Commun. (Cambridge, U.K.)* **2010**, *46*, 5021−5023.

(6) Liu, Y. D.; Xin, F.; Wang, F. M.; Luo, S. X.; Yin, X. H. Synthesis, Characterization, and Activities of Visible Light-Driven $Bi_2O_3$−$TiO_2$ Composite Photocatalysts. *J. Alloys Compd.* **2010**, *498*, 179−184.
(7) Bhande, S. S.; Mane, R. S.; Ghule, A. V.; Han, S. H. A Bismuth Oxide Nanoplate-Based Carbon Dioxide Gas Sensor. *Scr. Mater.* **2011**, *65*, 1081−1084.
(8) Orera, A.; Slater, P. R. New Chemical Systems for Solid Oxide Fuel Cells. *Chem. Mater.* **2010**, *22*, 675−690.
(9) Shuk, P.; Wiemhofer, H. D.; Guth, U.; Gopel, W.; Greenblatt, M. Oxide Ion Conducting Solid Electrolytes Based on $Bi_2O_3$. *Solid State Ionics* **1996**, *89*, 179−196.
(10) Kharton, V. V.; Marques, F. M. B.; Atkinson, A. Transport Properties of Solid Oxide Electrolyte Ceramics: A Brief Review. *Solid State Ionics* **2004**, *174*, 135−149.
(11) Hull, S. Superionics: Crystal Structures and Conduction Processes. *Rep. Prog. Phys.* **2004**, *67*, 1233−1314.
(12) Li, R.; Wang, D.; Ge, L.; He, S.; Chen, H.; Guo, L. Effect of $Bi_2O_3$ on the Electrochemical Performance of $LaBaCo_2O_{5+\delta}$ Cathode for Intermediate-Temperature Solid Oxide Fuel Cells. *Ceram. Int.* **2014**, *40*, 2599−2603.
(13) Elbatal, F. H. Gamma Ray Interaction with Bismuth Silicate Glasses. *Nucl. Instr. Methods Phys. Res., Sect. B* **2007**, *254*, 243−253.
(14) Bajaj, A.; Khanna, A.; Chen, B. G.; Longstaffe, J. G.; Zwanziger, U.-W.; Zwanziger, J. W.; Gómez, Y.; González, F. Structural Investigation of Bismuth Borate Glasses and Crystalline Phases. *J. Non-Cryst. Solids* **2009**, *355*, 45−53.
(15) Chanthima, N.; Kaewkhao, J.; Kedkaew, C.; Chewpraditkul, W.; Pokaipist, A.; Limsuwan, P. Study on Interaction of $Bi_2O_3$, PbO and BaO in Silicate Glass System at 662 keV for Development of Gamma-Rays Shielding Materials. *Progress in Nuclear Science and Technology*, Proceedings of the Fifth International Symposium on Radiation Safety and Detection Technology (ISORD-5), Kitakyushu, Japan, July 15−17, 2009; Atomic Energy Society of Japan: Tokyo, Japan, 2011; pp 106−109.
(16) Won-in, K.; Pongkrapan, S.; Dararutana, P. Eco-Glass Based on Thailand Quartz Sands and Bismuth Oxide. *Mater. Sci. Forum* **2011**, *695*, 223−226.
(17) Maeder, T. Review of $Bi_2O_3$ Based Glasses for Electronics and Related Applications. *Int. Mater. Rev.* **2013**, *58*, 3−40.
(18) Iyyapushpam, S.; Nishanthi, S. T.; Padiyan, D. P. Synthesis of Room Temperature Bismuth Oxide and Its Photocatalytic Activity. *Mater. Lett.* **2012**, *86*, 25−27.
(19) Cheng, L.; Kang, Y. Selective Preparation of $Bi_2O_3$ Visible Light-Driven Photocatalyst by Dispersant and Calcinations. *J. Alloys Compd.* **2014**, *585*, 85−93.
(20) Matsumoto, A.; Koyama, Y.; Tanaka, I. Structures and Energetics of $Bi_2O_3$ Polymorphs in a Defective Fluorite Family Derived by Systematic First-Principle Lattice Dynamics Calculation. *Phys. Rev. B: Condens. Matter Mater. Phys.* **2010**, *81*, 094117.
(21) Matsumoto, A.; Koyama, Y.; Togo, A.; Choi, M.; Tanaka, I. Electronic Structures Of Dynamically Stable $As_2O_3$, $Sb_2O_3$, and $Bi_2O_3$ Crystal Polymorphs. *Phys. Rev. B: Condens. Matter Mater. Phys.* **2011**, *83*, 214110.
(22) Harwig, H. A. On the Structure of Bismuthsesquioxide: $\alpha$, $\beta$, $\gamma$ and $\delta$-Phase. *Z. Anorg. Allg. Chem.* **1978**, *444*, 151−166.
(23) Sammes, N. M.; Tompsett, G. A.; Nafe, H.; Aldinger, F. Bismuth Based Oxide Electrolytes - Structure and Ionic Conductivity. *J. Eur. Cer. Soc.* **1999**, *19*, 1801−1826.
(24) Salazar-Pérez, A. J.; Camacho-López, M. A.; Morales-Luckie, R. A.; Sánchez-Mendieta, V.; Ureña-Núñez, F.; Arenas-Alatorre, J. Structural Evolution of $Bi_2O_3$ Prepared by Thermal Oxidation of Bismuth Nano-Particles. *Superficies Vacio* **2005**, *18* (3), 4−8.
(25) Nunn, S. D.; Payzant, E. A. Properties of Ionic-Conducting $\beta$-$Bi_2O_3$ Containing Mixed Dopants. *J. Am. Ceram. Soc.* **2002**, *85*, 2633−2636.
(26) Gomez, C. L.; Depablos-Rivera, O.; Medina, J. C.; Silva-Bermudez, P.; Muhl, S.; Zeinert, A.; Rodil, S. E. Stabilization of the Delta-Phase in $Bi_2O_3$ Thin Films. *Solid State Ionics* **2014**, *225*, 147−152.
(27) Yan, Y.; Zhou, Z.; Cheng, Y.; Qiu, L.; Gao, C.; Zhou, J. Template-Free Fabrication of $\alpha$- and $\beta$- $Bi_2O_3$ Hollow Spheres and Their Visible Light Photocatalytic Activity for Water Purification. *J. Alloys Compd.* **2014**, *605*, 102−108.
(28) Gualtieri, A. F.; Immovilli, S.; Prudenziati, M. Powder X-ray Diffraction Data for the New Polymorphic Compound $\omega$-$Bi_2O_3$. *Powder Diffr.* **1997**, *12*, 90−92.
(29) Kumada, N.; Kinomura, N. A New Allotropic Form of $Bi_2O_3$. *Mater. Res. Soc. Symp. Proc.* **1999**, *547*, 227−232.
(30) Ghedia, S.; Locherer, T.; Dinnebier, R.; Prasad, D. L. V. K.; Wedig, U.; Jansen, M.; Senyshyn, A. High-Pressure and High-Temperature Multianvil Synthesis of Metastable Polymorphs of $Bi_2O_3$: Crystal Structure and Electronic Properties. *Phys. Rev. B: Condens. Matter Mater. Phys.* **2010**, *82*, 024106.
(31) Locherer, T.; Dasari, L.; Prasad, V. K.; Dinnebier, R.; Wedig, U.; Jansen, M.; Garbarino, G.; Hansen, T. High-Pressure Structural Evolution of HP-$Bi_2O_3$. *Phys. Rev. B: Condens. Matter Mater. Phys.* **2011**, *83*, 214102.
(32) Chouinard, C.; Desgreniers, S. $Bi_2O_3$ under Hydrostatic Pressure: Observation of a Pressure-Induced Amorphisation. *Solid State Commun.* **2000**, *113*, 125−129.
(33) Pereira, A. L. J.; Errandonea, D.; Beltrán, A.; Gracia, L.; Gomis, O.; Sans, J. A.; García-Domene, B.; Miquel-Veyrat, A.; Manjón, F. J.; Muñoz, A.; Popescu, C. Structural Study of $\alpha$-Bi2O3 under Pressure. *J. Phys.: Condens. Matter* **2013**, *25*, 475402.
(34) Pereira, A. L. J.; Gomis, O.; Sans, J. A.; Pellicer-Porres, J.; Manjon, F. J.; Betran, A.; Rodriguez-Hernandez, P.; Muñoz, A. Pressure Effects on the Vibrational Properties of $\alpha$-$Bi_2O_3$: An Experimental and Theoretical Study. *J. Phys. Cond. Matter* **2014**, *26*, 225401.
(35) Cheng, H.; Huang, B.; Lu, J.; Wang, Z.; Xu, B.; Qin, X.; Zhang, X.; Dai, Y. Synergistic Effect of Crystal and Electronic Structures on the Visible-Light-Driven Photocatalytic Performances of $Bi_2O_3$ Polymorphs. *Phys. Chem. Chem. Phys.* **2010**, *12*, 15468−15475.
(36) Brezesinski, K.; Ostermann, R.; Hartmann, P.; Perlich, J.; Brezesinski, T. Exceptional Photocatalytic Activity of Ordered Mesoporous $\beta$-$Bi_2O_3$ Thin Films and Electrospun Nanofiber Mats. *Chem. Mater.* **2010**, *22*, 3079−3085.
(37) Li, M.; Li, F.; Yin, P. G. Tailoring the Band Structure of $\beta$-$Bi_2O_3$ by co-Doping for Realized Photocatalytic Hydrogen Generation. *Chem. Phys. Lett.* **2014**, *601*, 92−97.
(38) Fauth, F.; Peral, I.; Popescu, C.; Knapp, M. The New Material Science Powder Diffraction Beamline at ALBA Synchrotron. *Powder. Diffr.* **2013**, *28*, S360−S370.
(39) Mao, M. K.; Xu, J.; Bell, P. M. Calibration of the Ruby Pressure Gauge to 800 kbar under Quasi-Hydrostatic Conditions. *J. Geophys. Res.* **1986**, *91*, 4673−4676.
(40) Hammersley, A. P.; Svensson, S. O.; Hanfland, M.; Fitch, A. N.; Häusermann, D. Two-Dimensional Detector Software: From Real Detector to Idealized Image or Two-Theta Scan. *High Pressure Res.* **1996**, *14*, 235−248.
(41) Kraus, W.; Nolze, G. POWDER CELL - A Program for the Representation and Manipulation of Crystal Structures and Calculation of the Resulting X-Ray Powder Patterns. *J. Appl. Crystallogr.* **1996**, *29*, 301−303.
(42) Larson, A. C.; von Dreele, R. B. LANL Report 2004, 86−748.
(43) Toby, B. H. EXPGUI, A Graphical User Interface for GSAS. *J. Appl. Crystallogr.* **2001**, *34*, 210−213.
(44) Balic-Zunic, T.; Vickovic, I. IVTON - Program for the Calculation of Geometrical Aspects of Crystal Structures and Some Crystal Chemical Applications. *J. Appl. Crystallogr.* **1996**, *29*, 305−306.
(45) Debernardi, A.; Urlich, C.; Cardona, M.; Syassen, K. Pressure Dependence of Raman Linewidth in Semiconductors. *Phys. Status Solidi B* **2001**, *223*, 213−223.
(46) Hohenberg, P.; Kohn, W. Inhomogeneous Electron Gas. *Phys. Rev.* **1964**, *136*, 3864.
(47) Blöchl, P. E. Projector augmented-wave method. *Phys. Rev. B: Condens. Matter Mater. Phys.* **1994**, *50*, 17953−17979.

(48) Perdew, J. P.; Ruzsinszky, A.; Csonka, G. I.; Vydrow, O. A.; Suseria, G. E.; Constantin, L. A.; Zhou, X.; Burke, K. Restoring the Density-Gradient Expansion for Exchange in Solids and Surfaces. *Phys. Rev. Lett.* **2008**, *100*, 136406.
(49) Parlinski, K.; Li, Z. Q.; Kawazoe, Y. First-Principles Determination of the Soft Mode in Cubic $ZrO_2$. *Phys. Rev. Lett.* **1997**, *78*, 4063−4066.
(50) Efthimiopoulos, I.; Kemichick, J.; Zhou, X.; Khare, S. V.; Ikuta, D.; Wang, Y. High-Pressure Studies of $Bi_2S_3$. *J. Phys. Chem. A* **2014**, *118*, 1713−1720.
(51) Blower, S. K.; Greaves, C. The Structure of $\beta$-$Bi_2O_3$ from Powder Neutron Diffraction Data. *Acta Crystallogr.* **1988**, *44*, 587−589.
(52) Salazar-Pérez, A. J.; Camacho-López, M. A.; Morales-Luckie, R. A.; Sánchez-Mendieta, V.; Ureña-Ñúñez, F.; Arenas-Alatorre, J. Structural Evolution of $Bi_2O_3$ Prepared By Thermal Oxidation of Bismuth Nano-Particles. *Superficies Vacio* **2005**, *18* (3), 4−8.
(53) Monnereau, O.; Tortet, L.; Llewellyn, P.; Rouquerol, F.; Vacquier, G. Synthesis of $Bi_2O_3$ by Controlled Transformation Rate Thermal Analysis: A New Route for This Oxide? *Solid State Ionics* **2003**, *157*, 163−169.
(54) Chen, R.; Shen, Z.-R.; Wang, H.; Zhou, H.-J.; Liu, Y.-P.; Ding, D.-T.; Chen, T.-H. Fabrication of Mesh-Like Bismuth Oxide Single Crystalline Nanoflakes and Their Visible Light Photocatalytic Activity. *J. Alloys Compd.* **2011**, *509*, 2588−2596.
(55) Qiu, Y.; Yang, M.; Fan, H.; Zuo, Y.; Shao, Y.; Xu, Y.; Yang, X.; Yang, S. Nanowires of $\alpha$- and $\beta$-$Bi_2O_3$: Phase-Selective Synthesis and Application in Photocatalysis. *CrystEngComm* **2011**, *13*, 1843−1850.
(56) Ayala, A.; López-García, A.; Leyva, A. G.; de Benyacar, M. A. R. Stabilization of $\beta$-$Bi_2O_3$ by Hafnia. *Solid State Commun.* **1996**, *99*, 451−455.
(57) Jovalekic, C.; Zdujic, M.; Poleti, D.; Karanovic, L.; Mitric, M. Structural and Electrical Properties of the 2 $Bi_2O_3$·3$ZrO_2$ System. *J. Solid State Chem.* **2008**, *181*, 1321−1329.
(58) Akahama, Y.; Kawamura, H.; Singh, A. K. Equation of states of Bismuth to 222 GPa and Comparison of Gold and Platinum Pressure Scales to 145 GPa. *J. Appl. Phys.* **2002**, *92*, 5892−5897.
(59) Frogley, M. D.; Sly, J. L.; Dunstan, D. J. Pressure Dependence of the Direct Band Gap in Tetrahedral Semiconductors. *Phys. Rev. B: Condens. Matter Mater. Phys.* **1998**, *58*, 12579−12582.
(60) Pereira, A. L. J.; Gracia, L.; Santamaría-Pérez, D.; Vilaplana, R.; Manjón, F. J.; Errandonea, D.; Nalin, M.; Beltrán, A. Structural and Vibrational Study of Cubic $Sb_2O_3$ under High Pressure. *Phys. Rev. B: Condens. Matter Mater. Phys.* **2012**, *85*, 174108.
(61) Schneider, V. E.; Tornau, E. E. On the Theory of Isostructural Phase Transition in Crystals. *Phys. Status Solidi B* **1982**, *111*, 565−574.
(62) Pandey, K. K.; Poswal, H. K.; Kumar, R.; Sharma, S. M. High Pressure Iso-Structural Phase Transition in $BiMn_2O_5$. *J. Phys.: Condes. Matter* **2013**, *32*, 325401.
(63) Friedrich, A.; Juarez-Arellano, E. A.; Haussuhl, E.; Boehler, R.; Winkler, B.; Wiehl, L.; Morgenroth, W.; Burianek, M.; Muhlberg, M. Persistence of the Stereochemical Activity of the $Bi^{3+}$ Lone Electron Pair in $Bi_2Ga_4O_9$ up to 50 GPa and Crystal Structure of the High-Pressure Phase. *Acta Crystallogr., Sect. B: Struct. Sci.* **2010**, *66*, 323−337.
(64) Zunic, T. B.; Makovicky, E. Determination of the Centroid or 'The Best Centre' of a Coordination Polyhedron. *Acta Crystallogr., Sect. B: Struct. Sci.* **1996**, *52*, 78−81.
(65) Olsen, L. A.; López-Solano, J.; García, A.; Balic-Zunic, T.; Makovicky, E. Dependence of the Lone Pair of Bismuth on Coordination Environment and Pressure: An *ab Initio* Study on $Cu_4Bi_5S_{10}$ and $Bi_2S_3$. *J. Solid State Chem.* **2010**, *183*, 2133−2143.
(66) Lundegaard, L. F.; Makovicky, E.; Boffa-Ballaran, T.; Zunic, T. B. Crystal Structure and Cation Lone Electron Pair Activity of $Bi_2S_3$ between 0 and 10 GPa. *Phys. Chem. Miner.* **2005**, *32*, 578−584.
(67) Olsen, L. A.; Zunic, T. B.; Makovicky, E.; Ullrich, A.; Miletich, R. Hydrostatic Compression of Galenobismutite ($PbBi_2S_4$): Elastic Properties and High-Pressure Crystal Chemistry. *Phys. Chem. Miner.* **2007**, *34*, 467−475.
(68) Olsen, L. A.; Zunic, T. B.; Makovicky, E. High-Pressure Anisotropic Distortion of $Pb_3Bi_2S_6$: A Pressure-Induced, Reversible Phase Transition with Migration of Chemical Bonds. *Inorg. Chem.* **2008**, *47*, 6756−6762.
(69) Olsen, L. A.; Friese, K.; Makovicky, E.; Balic-Zunic, T.; Morgenroth, W.; Grzechnik, A. Pressure Induced Phase Transition in $Pb_6Bi_2S_9$. *Phys. Chem. Miner.* **2011**, *38*, 1−10.
(70) Friedrich, A.; Biehler, J.; Morgenroth, W.; Wiehl, L.; Winkler, B.; Hanfland, M.; Tolkiehn, M.; Burianek, M.; Mühlberg, M. High-Pressure Phase Transition of $Bi_2Fe_4O_9$. *J. Phys.: Condens. Matter* **2012**, *24*, 145401.
(71) Stoltzfus, M. W.; Woodward, P. M.; Seshadri, R.; Klepeis, J.-H.; Bursten, B. Structure and Bonding in $SnWO_4$, $PbWO_4$, and $BiVO_4$: Lone Pairs vs Inert Pairs. *Inorg. Chem.* **2007**, *46*, 3839−3850.
(72) Denisov, V. N.; Ivlev, A. N.; Lipin, A. S.; Mavrin, B. N.; Orlov, V. G. Raman Spectra and Lattice Dynamics of Single-Crystal $\alpha$-$Bi_2O_3$. *J. Phys.: Condens. Matter* **1997**, *9*, 4967−4978.
(73) Olijnyk, H.; Nakano, S.; Takemura, K. First- and Second Order Raman Scattering in Sb and Bi at High Pressure. *Phys. Status Solidi B* **2007**, *10*, 3572−3582.
(74) Lundegarrd, L. F.; Weck, G.; McMahon, M. I.; Desgreniers, S. Observation of an $O_8$ Molecular Lattice in the $\varepsilon$ Phase of Solid Oxygen. *Nature (London, U.K.)* **2006**, *443*, 201−204.
(75) Weck, G.; Loubeyre, P.; LeToullec, R. Observation of Structural Transition in Metal Oxygen. *Phys. Rev. Lett.* **2002**, *88*, 035504.
(76) Errandonea, D.; Manjón, F. J. On the Ferroelastic Nature of the Scheelite-to-Fergusonite Phase Transition in Orthotungstates and Orthomolybdates. *Mater. Res. Bull.* **2009**, *44*, 807−811.
(77) Dove, M. T. Theory of Displacive Phase Transitions in Minerals. *Am. Mineral.* **1997**, *82*, 213−244.